Matter

CellPress

Article

Accumulation-Driven Unified Spatiotemporal Synthesis and Structuring of Immiscible Metallic Nanoalloys

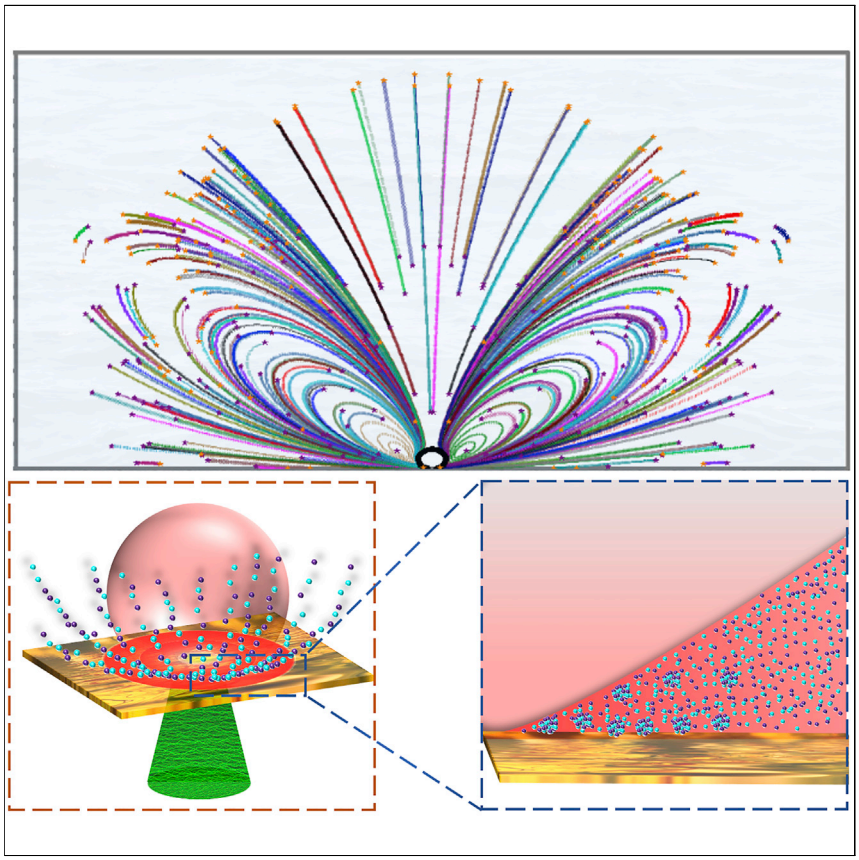

The concept of accumulation-mediated concentration is translated to the nano-/microscale to achieve *in situ* unified synthesis and structuring of immiscible nanoalloys. The confinement effect, high fluid flow, and site-specific heating at a laser-induced microbubble trap (MBT) results in one-shot RhAu alloying and structuring. Random walk simulations reveal enhanced millisecond-timescale concentration of ions in the MBT. The synthesized and structured RhAu nanoalloys demonstrate enhanced catalytic activity. Our generic strategy can be easily scaled up toward various catalytic and optoelectronic applications.

Benchmark
First qualification/assessment of material properties and/or performance

Bharath Bangalore Rajeeva, Pranaw Kunal, Pavana Siddhartha Kollipara, ..., Vaibhav Bahadur, Simon M. Humphrey, Yuebing Zheng

zheng@austin.utexas.edu

HIGHLIGHTS

Ultrafast simultaneous synthesis and structuring of immiscible nanoalloys (NAs)

Laser-mediated microbubble trap instantaneously accumulates the precursor ions

US^3 strategy reduces the synthesis timescale from minutes to milliseconds

RhAu NAs exhibit structure-property relationship and superior catalytic activity

Rajeeva et al., Matter *1*, 1606–1617
December 4, 2019
https://doi.org/10.1016/j.matt.2019.10.017

Matter

CellPress

Article

Accumulation-Driven Unified Spatiotemporal Synthesis and Structuring of Immiscible Metallic Nanoalloys

Bharath Bangalore Rajeeva,[1] Pranaw Kunal,[2,7] Pavana Siddhartha Kollipara,[3] Palash V. Acharya,[3] Minwoong Joe,[1,4] Matthew S. Ide,[5] Karalee Jarvis,[6] Yuanyue Liu,[1,3] Vaibhav Bahadur,[3] Simon M. Humphrey,[2] and Yuebing Zheng[1,3,6,8,*]

SUMMARY

Accumulation-mediated chemical reactions are a ubiquitous phenomenon in nature. Here, we explore microbubble-induced accumulation of precursor ions to achieve surfactant-free synthesis of immiscible metallic nanoalloys and simultaneously pattern the nanoalloys into targeted architectures for their enhanced catalytic applications. Our unified spatiotemporal synthesis and structuring (US^3) strategy, whereby millisecond-scale accumulation of the ions takes place in a highly confined laser-mediated microbubble trap (MBT), drives ultrafast alloy synthesis in sync with the structuring process. As a case in point, we employ the US^3 strategy for the *in situ* surfactant-free synthesis and patterning of traditionally immiscible rhodium-gold (RhAu) nanoalloys. Stochastic random walk simulations justify the millisecond-scale accumulation process, leading to a 3-order reduction in synthesis time. The catalytic activity and structure-property relationship were evaluated using the reduction of *p*-nitrophenol with $NaBH_4$. Our *in situ* synthesis and structuring strategy can be translated for high-throughput production and screening of multimetallic systems with tailored catalytic, optoelectronic, and magnetic functions.

INTRODUCTION

Accumulation-mediated concentration has been a ubiquitous phenomenon in nature to facilitate complex reactions, starting with the vital building blocks such as DNA and RNA that are essential for the emergence of early life.[1] The accumulation phenomenon has also been demonstrated to support formation of cell-like lipid vesicles,[2] induce proton gradients,[3] and enhance chemical reaction rates.[4] Multiple moieties such as ions and molecules can be triggered to move in response to an electrical or thermal gradient generated in scenarios ranging from nanoneedles to macroscale hydrothermal vents/cooling volcanic sites in geothermally heated porous rocks.[1,4] In particular, the accumulation via thermal gradients can significantly increase molecule concentration by a factor of 10^6.[1] In addition, ultrafast nucleation and a growth process reaching up to 10 μm/s can be realized upon accumulation of ions and molecules in confined spaces.[5]

Similar to the creation of complex multicomponent biological building blocks, the blending of multiple elements is an attractive strategy to tune the properties of inorganic materials via atomic ordering, size, and composition.[6,7] For instance, in a multimetallic nanoparticle (NP) system, d-band intermixing among the heteroatoms leads to a broader tuning of the chemical reactivity on the NP surface.[8] Bimetallic NP

Progress and Potential

The phenomenon of accumulation-mediated concentration has been crucial in the emergence of life. Complex reactions such as the synthesis of RNA/DNA are hypothesized to have resulted via precursor accumulation. Here, we translate the strategy to the nano-/microscale by using a laser-mediated microbubble trap (MBT) for the synthesis of immiscible metallic nanoalloys (NAs). Synthesis of immiscible NAs is difficult but highly desirable, because they manifest synergistic properties unseen in phase-segregated systems. We achieve *in situ* unified spatiotemporal synthesis and structuring (US^3) with millisecond-scale accumulation of precursor ions in an MBT leading to a 3-order reduction in synthesis time compared with the current protocols. Stochastic random walk simulations justify ultrafast accumulation, and the synthesized RhAu NAs exhibit superior catalytic activity. The US^3 strategy can be readily translated toward microfluidic device-integrated multicomponent systems for various applications.

alloys have been found to exhibit unique and significantly enhanced optical, electrical, and catalytic characteristics distinct from those of the pure metals.[9] Synthesis and fabrication of alloy metallic composites specifically composed of immiscible counterparts is highly desirable, as they manifest synergistic properties not seen in phase-segregated systems.[10–12]

Both traditional and unconventional protocols for immiscible nanoalloys require complex synthetic techniques, templates, and chemical precursors.[13] They typically involve encapsulation of precursor reagents with appropriate surfactants in confined spaces such as micelles,[14] dendrimers,[15] and femtodroplets,[16] as well as long thermal annealing at high temperatures. The resultant alloys possess excessive surfactants or coatings, which hinder their catalytic performance.[17] Light-induced nucleation provides an attractive approach to nucleating and crystallizing multielement materials in solutions with a high spatiotemporal control.[18] Liquid-phase laser synthesis requires no surfactants, leading to ligand-free NPs.[17,19,20] Here, we exploit the integration of accumulation-mediated concentration and laser-induced nucleation to enable the simultaneous synthesis and structuring of metallic alloys. An ultrahigh precursor supersaturation along with light-controlled temperature gradient and microbubble trap (MBT) leads to nucleation and growth of immiscible nanoalloys.

As a case in point, we demonstrate the *in situ* unified synthesis and structuring (US^3) of classically immiscible rhodium-gold nanoalloys (RGNs). RGNs are challenging systems to synthesize, with the phase diagrams of these alloys predicting no stable regions below 2,139 K and 1.0 atm.[21] By harnessing the confinement effect, high fluid flow, and site-specific heating at a laser-induced MBT, we achieve one-shot RhAu alloying and structuring. Random walk (RW) simulations reveal enhanced concentration of ions in the vicinity of the MBT within a milliseconds time frame. The ion supersaturation leads to the high-throughput synthesis strategy with ~3 orders of reduction in the critical radius and synthesis time. The ultrafast nucleation and growth process occurs on the millisecond regime and enables time-synchronized low-power synthesis and structuring of surfactant-free RGNs. We are able to modulate the density of the alloys over the substrate via control of substrate stage by computer programming. Furthermore, we demonstrate the catalytic activity of the fabricated RhAu structures using reduction of *p*-nitrophenol to *p*-aminophenol by $NaBH_4$ as a model study, and demonstrate a structure-property relationship based on the modulated density of alloys. The fabricated structures of alloys possess superior catalytic performance compared with individual counterparts. With advantages such as simplified manufacturing process, ultrafast nucleation time with micro-/nanoscale reaction confinement, and structuring of thermodynamically challenging immiscible nanoalloys, US^3 provides a way to fabricate and screen a variety of new materials for superior functionalities.

RESULTS AND DISCUSSION

The unification of synthesis and printing steps depends on combined occurrence of site-specific ultrafast nucleation and growth, large thermal gradients, and precursor supersaturation. The US^3 strategy achieves all these criteria within milliseconds using a thermoplasmonic Au nanoisland (AuNI) substrate capable of attaining laser-induced highly confined thermal gradient in the vicinity of an MBT. Figure 1A shows the fabrication setup and concept on US^3, whereby the precursor solution consisting of an equimolar mixture of $RhCl_3$ and $HAuCl_4$ is present over an AuNI substrate. Upon the incidence of a low-power ($\approx$0.6 mW/μm^2) continuous-wave (CW) laser

[1]Materials Science and Engineering Program, Texas Materials Institute, The University of Texas at Austin, Austin, TX 78712, USA

[2]Department of Chemistry, The University of Texas at Austin, Austin, TX 78712, USA

[3]Walker Department of Mechanical Engineering, The University of Texas at Austin, Austin, TX 78712, USA

[4]School of Mechanical Engineering, Sungkyunkwan University, Suwon, Gyeonggi-do 16419, South Korea

[5]ExxonMobil Research and Engineering Company, Annandale, NJ 08801, USA

[6]Texas Materials Institute, The University of Texas at Austin, Austin, TX 78712, USA

[7]Oak Ridge National Laboratory, P.O. Box 2008, MS6472, Oak Ridge, TN 37831-6472, USA

[8]Lead Contact

*Correspondence: zheng@austin.utexas.edu

https://doi.org/10.1016/j.matt.2019.10.017

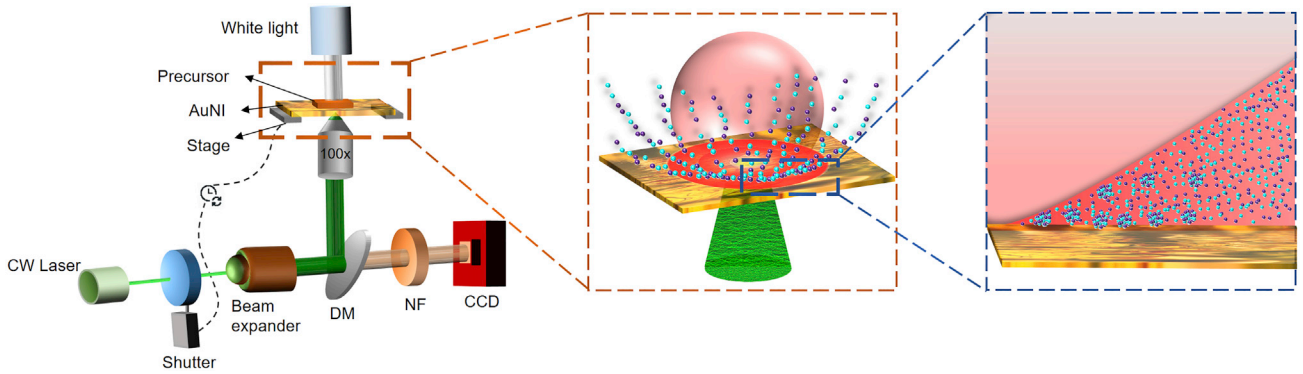

Figure 1. Schematic Demonstrating the Optical Setup and Ion-Accumulation Aspect of the US^3 Strategy

The laser-induced MBT can lead to highly localized supersaturations of precursor ions near the substrate, enabling the simultaneous synthesis and structuring of immiscible alloys.

beam (532 nm) through a high-magnification objective, the AuNIs excited on resonance re-emit the energy via nonradiative Landau damping, which results in intense localized thermal gradients and eventually leads to the formation of MBT.[22] The Marangoni-convection-mediated ultrafast accumulation (see US^3 Mechanism for more details) at the MBT-substrate interface leads to reduction of the ions from the precursor solution and eventual structuring of the RGNs.

For catalytic applications of structured alloys, it is desirable to achieve modular patterning independence and versatility along with high resolution to attain maximum surface areas. In addition to the high surface-to-volume ratio, micropatterning enables new catalyst designs and less catalyst loading, which translates into process intensification and cost savings. To achieve structuring of the RGNs, we employed a combination of the stage translation and shutter activation/deactivation. Figure 2A shows the low-magnification image of RGNs structured on the substrate with interline spacing of 4 μm at a stage speed of 30 μm/s while the inset shows a complete fabricated sample of 2.25 mm^2 in area. To achieve the modulation of the structured RGN density, we fabricated preprogrammed patterns with interline spacings from 2 to 8 μm (Figures 2B–2D and Video S1). As the stage traverses, the synthesized RGNs are instantaneously deposited along the contact line of the MBT due to a combination of van der Waals attraction and force balance on the bubble interface.[23–28] Large-area optical profilometry reveals the structuring confinement and uniform deposition of the RGNs with an average height of 44.9 $\pm$ 5.1 nm (Figure S1). The height profile is further confirmed by atomic force microscopy (AFM) imaging, which shows a characteristic half-ring morphology supporting the immobilization of reaction product at the MBT-substrate contact line (Figure S2). In addition, the realization of submicron linewidths can provide advantages in terms of surface area, which can be harnessed for enhanced applications through nanoscale design.[29] The MBT-mediated immobilization leads to tunable submicron linewidths based on the stage speed, with lower linewidths observed as the speed increases (Figure 2E).

To further validate the RGN synthesis process, we performed high-resolution transmission electron microscopy (HRTEM) imaging by transferring the particles onto a TEM grid (see Experimental Procedures for details). The presence of the AuNI substrate can provide heterogeneous nucleation sites, with initial nucleation likely occurring over the substrate.[30] These RGNs were highly crystalline in nature as confirmed by HRTEM analysis whereby a mixture of well-defined lattice planes

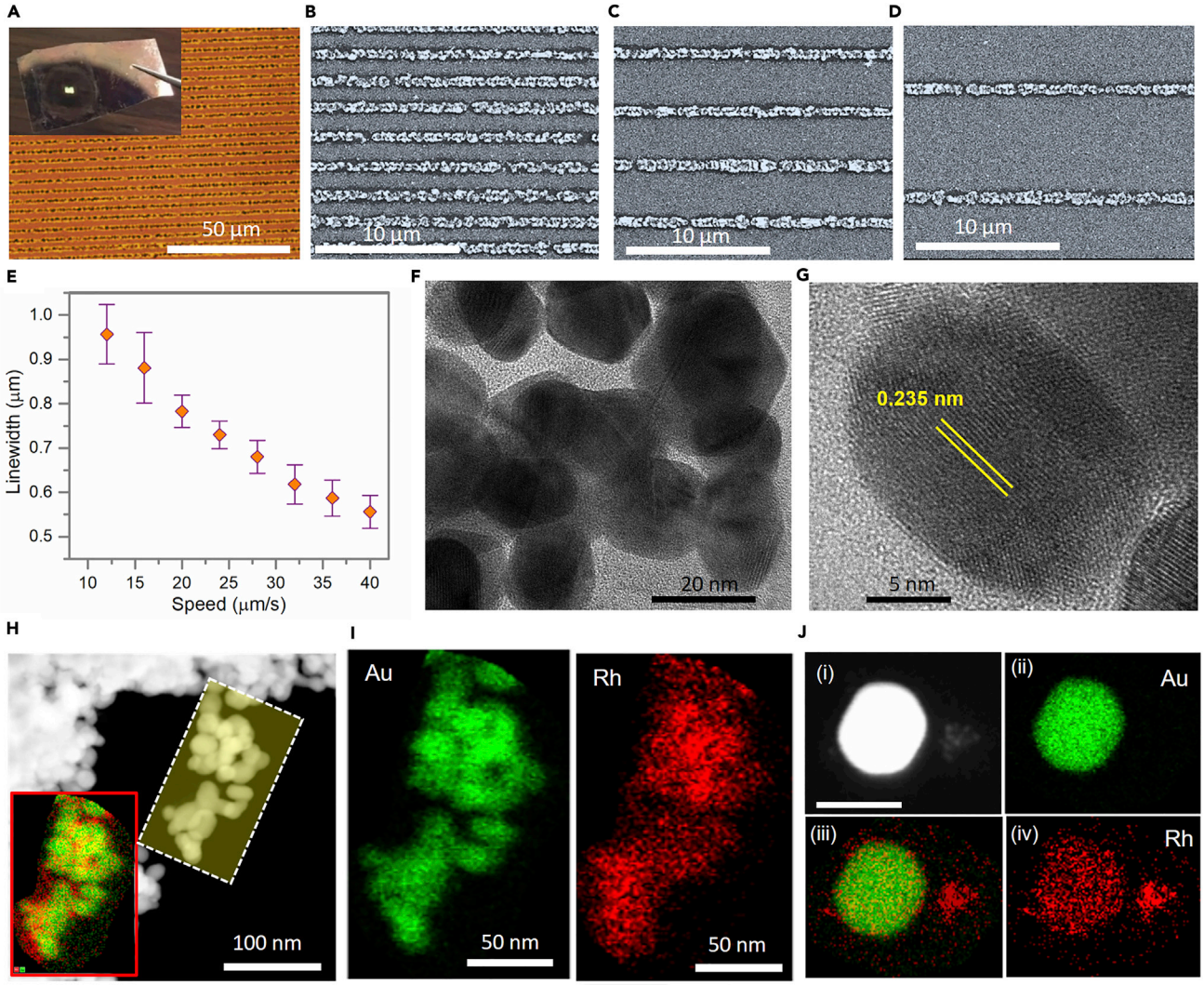

Figure 2. RGN Synthesis and Characterization

(A) Bright-field optical image of the RGNs fabricated using US[3] strategy. The inset shows a completed sample of 2.25-mm^2 area. The bright reflection observed is due to the diffraction effect from the closely printed RGN lines.

(B–D) Scanning electron microscopy (SEM) images of the printed RGNs with (B) 2-μm, (C) 4-μm, and (D) 8-μm interline spacings.

(E) Tunable submicron linewidth of the structured RGNs as a function of the stage translation speed. When the translation speed is increased continuously, a gradual reduction in the linewidth is observed.

(F and G) High-resolution transmission electron microscopy (HRTEM) images of the transferred RGNs showing the crystallinity (F) and the d lattice spacing (G) of RGN.

(H) HAADF-STEM image of the transferred RGNs, along with the inset of a two-dimensional (2D) overlapped energy-dispersive X-ray spectroscopy (EDS) mapping of Rh and Au.

(I) Segregated Rh and Au 2D EDS mapping results showing the distribution of both the elements.

(J) HRTEM image (i) and 2D EDS mapping showing Au only (ii), Au+Rh overlaid (iii), and Rh only (iv) intensities of a single RGN. Scale bar, 25 nm.

was seen. The images show that the particles are predominantly cuboctahedral with various degrees of truncation (Figure 2F). Measured $d_{<111>}$ from various regions of interest showed increased d spacing between 0.23 and 0.235 nm (Figure 2G), pointing toward an overall face-centered cubic structure. In comparison, Figures S3B and S3C show the nonalloyed Rh clusters exhibiting a d spacing of 0.217 nm (theoretical Rh $d_{<111>}$ 0.219 nm). The multiple nuclei created via ultrahigh supersaturation results in a small number of nonalloyed Rh particles (Figures S3A–S3C) besides relatively large-sized RGNs.[8,31] These observations are in agreement with what has been

reported previously, whereby surface segregation of Rh was also observed for RGNs synthesized using microwave heating.[8]

High-angle annular dark-field scanning transmission electron microscopy (HAADF-STEM) imaging and energy-dispersive X-ray spectroscopy (EDS) analysis of RGNs show that Rh and Au are homogeneously alloyed with an Rh/Au molar ratio of 0.03 (Figures 2H–2J) (see US^3 Mechanism for more details regarding Rh/Au ratio). Low-resolution TEM imaging of RGNs reveal a pseudo-Gaussian distribution of particle sizes with an average size of 24.62 $\pm$ 6.38 nm (Figure S4). Scanning electron microscopy (SEM) and EDS imaging of the structured RGNs shows the confinement of the reaction to the lines traversed by the incident laser (Figure S5A). Furthermore, X-ray photon spectroscopy (XPS) analysis of RGNs showed that successful reduction of both Rh^{3+} and Au^{3+} indeed occurred using the US^3 strategy discussed herein. For Rh, peaks corresponding to only Rh(0) are observed, whereas a small fraction of Au(I) (a side product of Au^{3+} reduction) is also detected (Figure S5B). To validate the uniformity of the US^3 process, we obtained a transmission spectrum of the sample at random locations with 200-μm spacing. The consistent spectra of the various sites with a narrow transmission dip of 561.46 $\pm$ 1.52 nm confirm the large-area structuring uniformity (Figure S5C).

US^3 Mechanism

The prerequisite of the US^3 strategy is to attain ultrafast supersaturation at the MBT. The ion-accumulation phenomenon is simulated using RW simulation. RW processes are one of the fundamental types of stochastic processes, with applications in neuron studies and operations theory, among others.[32] RW has been used to study processes under thermal gradients, such as to determine the concentration increment of protobiomolecules toward high molecular aggregation,[1] and to determine pH cycling statistics.[3] Our temperature and flow profile around the MBT were simulated using existing modules in COMSOL (Figures 3A and 3B) (see Supplemental Information for more details). Upon MBT generation, three primary phenomena influence the flow of ions in the solution: (1) Rayleigh-Bernard convection velocity due to solution density gradient, (2) Marangoni convection velocity due to bubble surface tension gradient, and (3) thermophoretic drift velocity from inherent thermal gradient, an effect known as the Ludwig-Soret effect.[33] An angular-dependent comparison reveals that Marangoni convection dominates in the vicinity of the MBT, while the thermophoretic drift velocity is at least two orders of magnitude less than the other individual components of the flow velocity (Figures S6A–S6H).

The flow profile is then imposed onto the ions and their trajectory is noted using RW simulation. For determination of the concentration of ions near the bubble, the flow profile that is obtained from COMSOL simulations is incremented with Brownian motion and incremental displacement is evaluated using Equation 1:

$$\Delta s(r,z) = \sqrt{4D\Delta t}\eta(t) + \{v(r,z) + D * S_T * \nabla T(r,z)\}\Delta t, \qquad \text{(Equation 1)}$$

where $\Delta s(r,z)$ is the displacement of ion in a unit time step Δt, D is the diffusion coefficient, $\eta(t)$ is the viscosity, S_T is the Soret coefficient, $v(r,z)$ is the convective velocity at a given position, and ∇T is the gradient of temperature. Since the Marangoni velocity spans over several orders of magnitude (0.1 μm/s to 0.8 m/s), a dynamic time step is chosen to be inversely proportional to the velocity that the ion experiences at given spatial coordinates (see Supplemental Information for details). The ion-accumulation statistics in the 300-ms time frame are inferred from 5,000 particles randomly distributed in 25 × 25-μm^2 area (Figure S7). Figure 3C shows a random selection of 200 ions and their simulated trajectories, while the ion trajectory in

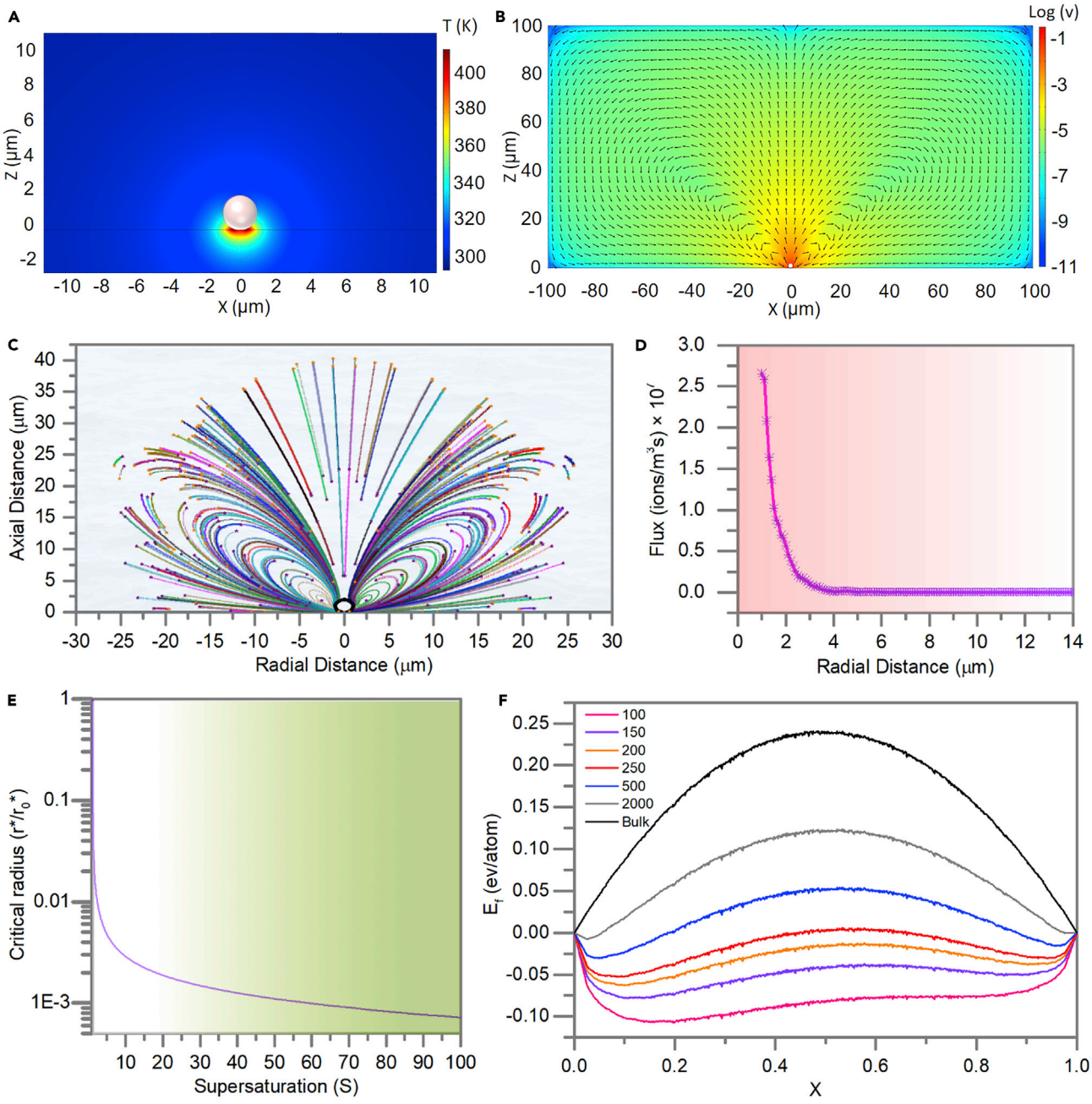

Figure 3. US³ Mechanism and Simulation

(A) Simulated temperature distribution in the vicinity of an MBT. The radius of the bubble is 1 μm.

(B) Simulated flow velocity distribution around MBT with logarithmic scale in a cross-sectional view.

(C) Trajectory of 200 ions simulated using the random walk simulations for a total duration of 300 ms, showing the concentration of ions at the MBT/substrate interface.

(D) The calculated incident ion flux, showing an exponential increase in the close vicinity of the MBT required to supplement the reduced ions.

(E) The normalized critical nuclear radius as a function of supersaturation *S*, demonstrating a 3-order reduction in the radius.

(F) The heat of formation E_f for RGNs at different Rh atomic concentration *x* and total number of atoms of the NPs.

Video S2 shows the crucial role of Marangoni convection toward ultrafast accumulation. As the ions come closer to the three-phase contact (TPC) line (air/substrate/water), surface and capillary forces dominate within ~200 nm of the bubble,

attracting the particles toward the TPC line.[34,35] In addition, near the MBT, counteracting Marangoni and capillary forces eventually lead to a stagnation point on the bubble surface, where the velocity of the flow is zero under the bubble and the particles reaching beyond this point head toward the TPC line.[36,37] By incorporating the stagnation phenomenon and the flow profile in RW simulation, an ultrahigh supersaturation ratio of 27.2 $\pm$ 1.48 is observed. Furthermore, the ion flux toward the MBT plays an important role in supersaturation, which increases linearly with the supply rate of ions.[38] An exponential increase in the flux is observed in the vicinity of the MBT, helping maintain a high supersaturation value (Figure 3D).

The MBT generation process is fast (<10 ms) and, post MBT generation, the ions from within 10-μm vicinity reach the MBT in less than 1 ms (Figure S8). Instantaneous high ion saturation in conjunction with elevated temperature at the MBT provides an ideal environment for the synthesis of RGNs. The overall net free energy change accompanying the nucleation process can be expressed as the sum of a surface free energy term (ΔG_s) and a volumetric free energy term (ΔG_v),[30] according to Equation 2:

$$\Delta G(r) = \Delta G_s + \Delta G_v = 4\pi r^2\gamma - \frac{4}{3}\pi r^3 \frac{RT\ln(S)}{V_m}, \qquad \text{(Equation 2)}$$

where γ is the surface free energy per unit area, R is the universal gas constant, r is the NP radius, T is the temperature in Kelvin, S is the supersaturation ratio defined as the ratio of the number densities of the nucleating phase in the bulk and at coexistence, and V_m is the molar volume of the nucleating phase.[30] Since the volumetric and surface free energy terms are negative and positive in nature, respectively, there exists a critical radius (r_c), which is defined as a metastable state wherein any infinitesimal positive/negative variation from the critical radius will lead to a continuous growth/dissolution of the nucleating phase. A smaller value of critical radius therefore translates to an increased probability for nucleation. The critical radius can be expressed as

$$r* = \frac{2\gamma V_m}{RT\ln(S)}. \qquad \text{(Equation 3)}$$

Herein we plot the normalized critical radius for RGNs as a function of supersaturation (S). As seen in Figure 3E, the critical radius shows an exponential decrease with increasing S. A supersaturation of $S \approx 27$ present in the asymptotic region results in the most favorable thermodynamic conditions for nucleation. An incremental change in the supersaturation ratio in the asymptotic region would lead to a minimal decrease in the critical radius, and therefore the probability for nucleation would be very high at $S \approx 27$. Furthermore, we evaluate the alloying ability by calculating the heat of formation (E_f) for RGNs of different sizes from their monometallic constituents using a thermodynamic model and the modified embedded atom method (MEAM).[39] The E_f for the RGNs under the assumption of homogeneously disordered NPs can be expressed as a function of the cohesive energies of its constituent elemental bulk and bulk alloy as

$$E_f^{p\ A-B} = E_f^{b\ A-B}\left(1-\sqrt[3]{\frac{1}{N}}\right) - (1-x)E_c^{bA}\left(1-\sqrt[3]{\frac{1}{N(1-x)}}\right) - xE_c^{bB}\left(1-\sqrt[3]{\frac{1}{Nx}}\right). \qquad \text{(Equation 4)}$$

Here, E_f represents the formation energy for an alloy particle containing N number of atoms (Au and Rh represented as A and B, respectively) with x being the chemical concentration of Rh in the RGN. The superscripts p and b represent the cohesive energy (E_c) of NP and bulk alloy, respectively. The cohesive energies of the bulk alloy at

x were calculated using MEAM interatomic potential for the RhAu system.[40] The heat of formation shows a clear enhancement of alloying ability for all the range of Rh atomic concentrations *x* with decreasing total number of atoms (Figure 3F). At the initial growth stage, a negative heat of formation is obtained in full range of *x*, implying the favorability of RGN synthesis. In particular, the Au-rich region has more capability to accommodate RGN synthesis since the heat of formation is the lowest in this regime, which corroborates with Au-rich RGNs observed in the experimental results (Figure 2H). Since the MBT provides a microsized reaction region close to the TPC and convection-driven currents promote instantaneous supersaturation of the ions, spontaneous alloying of the NPs at lower temperatures is enabled. The RGN synthesis is driven primarily by the accumulation of ions at the MBT, while the elevated temperature due to laser absorption in the MBT's vicinity supplements the synthesis. After synthesis, the RGNs are structured on the substrate as per this mechanism. These results reveal that the RGN synthesis shifts from a temperature-driven phenomenon at the bulk scale to a coalescence-driven phenomenon at the nanoscale.

The catalytic applications of metal nanoalloys have attracted significant interest.[16,41–43] Specifically, RGNs have been established to exhibit enhanced activity in comparison with individual Rh and Au components in reduction reactions.[8,44] To evaluate the activity of the fabricated RGNs via US^3, we prepared millimeter-scale arrays of RGNs (Figure 2A, inset) along with pristine Rh and Au substrates, and used them to catalyze the well-studied reduction of *p*-nitrophenol with $NaBH_4$. The pristine Rh substrate was fabricated by employing only $RhCl_3$ in the precursor solution. All the nanoparticle substrates showed reduction in activity, with the conversion using the RGNs being the highest (Figures 4A and 4B). The solution UV-visible spectrum was used to track the depletion of *p*-nitrophenol. During the fabrication, the RGNs adhered strongly to the substrates and virtually no RGN leaching was observed (Figure S9). Furthermore, we explored the structure-property relationship by using US^3 to fabricate millimeter-scale RGNs with varied line spacing of 2 μm, 4 μm, and 8 μm. The EDS spectra normalized with the Au peak shows reduction in the quantity of RGNs with increasing line spacing (Figure 4C). This modulation is manifested in the catalytic performance, with the RGNs with a spacing of 2 μm showing the highest activity (Figure 4D). These results confirm US^3 to be a feasible strategy to unify the synthesis and structuring of nanoalloys for catalytic applications.

In summary, we have successfully demonstrated the US^3 strategy for *in situ* synthesis and structuring of catalytically active RGNs. To unify these discrete aspects, we synergize the ion-accumulation effect, high fluid flow velocity, and site-selective temperature increment of a laser-induced MBT. HRTEM imaging reveals the complete mixing of the elements as well as their crystalline nature. RW and modified MEAM simulations justify the ion-accumulation effect, and the subsequent multiple-order-of-magnitude reduction in the synthesis time. The structured RGNs are utilized for the reduction of *p*-nitrophenol with enhanced catalytic activity. With its unique advantages in *in situ* synthesis and structuring and avoidance of surfactants, our US^3 strategy is promising for high-throughput development and screening of various multielement nanomaterials with desired catalytic, optical, electronic, and magnetic functions.

EXPERIMENTAL PROCEDURES

US^3 Sample Fabrication

The US^3 process was performed by a time-synched integration of the stage translation and shutter activation/deactivation. To prepare the thermoplasmonic substrates, we deposited 4-nm Au film on a glass substrate using thermal deposition

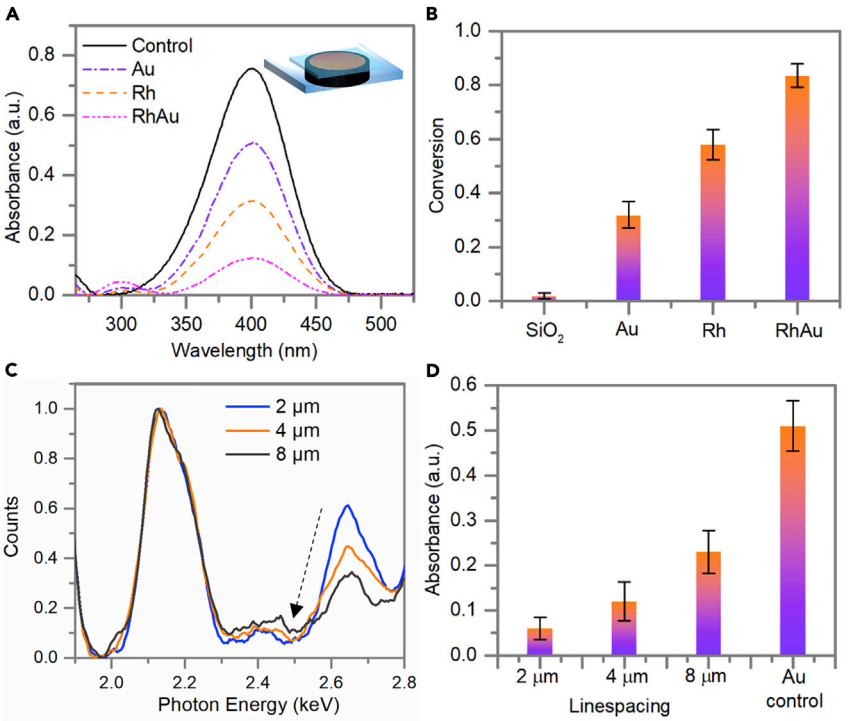

Figure 4. Catalytic Studies

(A) UV-visible absorption spectra showing the reduction of *p*-nitrophenol catalyzed by the structured RGNs, Rh, and Au substrates, as well as control *p*-nitrophenol solution. The inset shows the configuration wherein a 30-μL droplet is confined within a chamber to avoid evaporation. The product and reactant peaks are at 296 nm and 400 nm, respectively.

(B) Conversation percentage of the reactants catalyzed by control samples (SiO_2, Rh, and Au) and the RGNs.

(C) EDS spectra of RGNs fabricated via US[3] with 2-μm, 4-μm, and 8-μm line spacing. The spectra are normalized with respect to Au peak.

(D) Catalytic dependence of the RGNs on the line spacing as characterized using the 400-nm reactant peak. A higher conversion (corresponding to lower reactant absorbance) is observed when the line spacing is reduced.

(Denton Thermal evaporator) at a base pressure of 9×10^{-6} torr. The sample was subsequently annealed at 550°C for 2 h. The precursor aqueous solutions consisted of equal proportions of 0.02 M $RhCl_3$ and 0.02 M $HAuCl_4$. The solution was placed on the substrate using a micropipette and confined within a 500-μm-thick spacer (Figure S2A). A CW laser (532 nm) was focused using a high-magnification objective (spot size = 1 μm) to achieve the MBT. Post-MBT generation, the structuring process via synchronized stage translation and shutter operation, was monitored in real time through a CCD camera with a white-light source illuminating the substrate from the top. A Prior Proscan Scientific Stage (x-y resolution = 14 nm) was used, while a motorized flipper (ThorLabs MFF102) acted as a shutter. The response time of the flipper is 500 ms. To modulate the quantity of RGNs on the substrate, the stage moved along the predetermined (x, y) coordinates with an on/off status of the shutter for each coordinate. After the structuring process, the substrate was thoroughly washed and dried under nitrogen flow.

Structural and Chemical Characterization

SEM images were obtained using an FEI Quanta 650 scanning electron microscope, while the high-resolution AFM images were taken with a Park Scientific atomic force

microscope in the non-contact mode. A thin gold layer was sputter coated for taking SEM images and large-area EDS mapping to avoid charging. Large-area height profile was obtained using a Wyko NY9100 optical profilometer. XPS measurements were performed using a Kratos X-Ray Photoelectron Spectrometer-Axis Ultra DLD machine over a 300 × 500-μm^2 area. To obtain the TEM images, we physically transferred the structured sample onto a 200-mesh copper Formvar (Ted Pella) TEM grid. This was achieved by scraping the TEM grid against the structured substrate. Low-resolution TEM images were obtained using an FEI Tecnai transmission electron microscope, while the high-resolution TEM images, HAADF-STEM images, and EDS spectra were acquired using a JEOL 2010F transmission electron microscope equipped with an Oxford EDS detector. The instrument was operated at 200 keV with a 0.19-nm point-to-point resolution. The lattice spacing values were calculated using fast Fourier transform.

Simulations

Multiple commercial software packages such as COMSOL, MATLAB, and LAMMPS were utilized to perform the temperature profile, flow profile, stochastic RW, and molecular dynamics simulations. Please refer to Supplemental Information for more details of the formulations for each case.

Catalytic Studies

The catalytic activity of RGNs and control substrates was measured by drop casting 15 μL of aqueous *p*-nitrophenol solution (1.5 mmol/L) and 15 μL of freshly prepared aqueous $NaBH_4$ solution (750 mmol/L) onto the millimeter-scale substrate. The drop was confined within a spacer to minimize water evaporation, and the reaction was allowed to proceed for 1 h at room temperature. After completion, the droplet was collected and an additional 470 μL of deionized water was added to rinse the substrate and dilute the droplet. The final solution was transferred to a quartz cuvette to collect UV-visible absorption spectra (Genesys; Thermo Fisher). The change in the absorption at 400 nm was used to quantify reaction conversion.

SUPPLEMENTAL INFORMATION

Supplemental Information can be found online at https://doi.org/10.1016/j.matt.2019.10.017.

ACKNOWLEDGMENTS

B.B.R., P.S.K., and Y.Z. acknowledge the financial support of the National Science Foundation (NSF-CMMI-1761743), ExxonMobil Research and Engineering Company (UTA17-000828), and National Aeronautics and Space Administration (NASA: 80NSSC17K0520). P.K. and S.M.H. acknowledge the financial support of the National Science Foundation (NSF-CHE-1807847). M.J. acknowledges the National Research Foundation of Korea (NRF-2016R1A6A3A11934734) and the KISTI grant (KSC-2015-C2-021). P.V.A. and V.B. acknowledge the financial support of the National Science Foundation (NSF-1653412). We thank Zhiyao Duan and Graeme Henkelman for providing the MEAM potentials and Eric Sikma for assistance with the catalytic measurements.

AUTHOR CONTRIBUTIONS

B.B.R. and Y.Z. conceived the idea and designed the experiments. P.K., M.S.I., and S.M.H. assisted in sample preparation and catalytic studies. P.S.K., P.V.A., M.J., B.B.R., Y.L., and V.B. worked on the simulations. P.K. and K.J. worked on the TEM

measurement and analysis. B.B.R. conducted the experiments. All authors contributed to writing and proofreading the manuscript.

DECLARATION OF INTERESTS

The authors declare no competing interests.

Received: April 3, 2019
Revised: July 31, 2019
Accepted: October 15, 2019
Published: November 6, 2019

REFERENCES

1. Keil, L., Hartmann, M., Lanzmich, S., and Braun, D. (2016). Probing of molecular replication and accumulation in shallow heat gradients through numerical simulations. Phys. Chem. Chem. Phys. *18*, 20153–20159.

2. Budin, I., Bruckner, R.J., and Szostak, J.W. (2009). Formation of protocell-like vesicles in a thermal diffusion column. J. Am. Chem. Soc. *131*, 9628–9629.

3. Keil, L.M.R., Moller, F.M., Kiess, M., Kudella, P.W., and Mast, C.B. (2017). Proton gradients and pH oscillations emerge from heat flow at the microscale. Nat. Commun. *8*, 1897.

4. Liu, M., Pang, Y.J., Zhang, B., De Luna, P., Voznyy, O., Xu, J.X., Zheng, X.L., Dinh, C.T., Fan, F.J., Cao, C.H., et al. (2016). Enhanced electrocatalytic CO_2 reduction via field-induced reagent concentration. Nature *537*, 382–386.

5. Grossier, R., Magnaldo, A., and Veesler, S. (2010). Ultra-fast crystallization due to confinement. J. Cryst. Growth *312*, 487–489.

6. He, R., Wang, Y.C., Wang, X.Y., Wang, Z.T., Liu, G., Zhou, W., Wen, L.P., Li, Q.X., Wang, X.P., Chen, X.Y., et al. (2014). Facile synthesis of pentacle gold-copper alloy nanocrystals and their plasmonic and catalytic properties. Nat. Commun. *5*, 4327.

7. Ferrando, R., Jellinek, J., and Johnston, R.L. (2008). Nanoalloys: from theory to applications of alloy clusters and nanoparticles. Chem. Rev. *108*, 845–910.

8. Garcia, S., Zhang, L., Piburn, G.W., Henkelman, G., and Humphrey, S.M. (2014). Microwave synthesis of classically immiscible rhodium-silver and rhodium-gold alloy nanoparticles: highly active hydrogenation catalysts. ACS Nano *8*, 11512–11521.

9. Swiatkowska-Warkocka, Z., Pyatenko, A., Krok, F., Jany, B.R., and Marszalek, M. (2015). Synthesis of new metastable nanoalloys of immiscible metals with a pulse laser technique. Sci. Rep. *5*, 9849.

10. Wang, D., Villa, A., Porta, F., Prati, L., and Su, D.S. (2008). Bimetallic gold/palladium catalysts: correlation between nanostructure and synergistic effects. J. Phys. Chem. C *112*, 8617–8622.

11. Kunal, P., Roberts, E.J., Riche, C.T., Jarvis, K., Malrnstadt, N., Brutchey, R.L., and Humphrey, S.M. (2017). Continuous flow synthesis of Rh and RhAg alloy nanoparticle catalysts enables scalable production and improved morphological control. Chem. Mater. *29*, 4341–4350.

12. Yao, Y., Huang, Z., Xie, P., Lacey, S.D., Jacob, R.J., Xie, H., Chen, F., Nie, A., Pu, T., Rehwoldt, M., et al. (2018). Carbothermal shock synthesis of high-entropy-alloy nanoparticles. Science *359*, 1489–1494.

13. Essinger-Hileman, E.R., DeCicco, D., Bondi, J.F., and Schaak, R.E. (2011). Aqueous room-temperature synthesis of Au-Rh, Au-Pt, Pt-Rh, and Pd-Rh alloy nanoparticles: fully tunable compositions within the miscibility gaps. J. Mater. Chem. *21*, 11599–11604.

14. Yonezawa, T., and Toshima, N. (1993). Polymer-protected and micelle-protected gold platinum bimetallic systems - preparation, application to catalysis for visible-light-induced hydrogen evolution, and analysis of formation process with optical methods. J. Mol. Catal. *83*, 167–181.

15. Endo, T., Fukunaga, T., Yoshimura, T., and Esumi, K. (2006). Scavenging DPPH radicals catalyzed by binary noble metal-dendrimer nanocomposites. J. Colloid Interface Sci. *302*, 516–521.

16. Chen, P.C., Liu, G.L., Zhou, Y., Brown, K.A., Chernyak, N., Hedrick, J.L., He, S., Xie, Z., Lin, Q.Y., Dravid, V.P., et al. (2015). Tip-directed synthesis of multimetallic nanoparticles. J. Am. Chem. Soc. *137*, 9167–9173.

17. Zhang, D.S., Goekce, B., and Barcikowski, S. (2017). Laser synthesis and processing of colloids: fundamentals and applications. Chem. Rev. *117*, 3990–4103.

18. Tominaga, Y., Maruyama, M., Yoshimura, M., Koizumi, H., Tachibana, M., Sugiyama, S., Adachi, H., Tsukamoto, K., Matsumura, H., Takano, K., et al. (2016). Promotion of protein crystal growth by actively switching crystal growth mode via femtosecond laser ablation. Nat. Photon. *10*, 723–726.

19. Rajeeva, B.B., Wu, Z.L., Briggs, A., Acharya, P.V., Walker, S.B., Peng, X.L., Bahadur, V., Bank, S.R., and Zheng, Y.B. (2018). "Point-and-shoot" synthesis of metallic ring arrays and surface-enhanced optical spectroscopy. Adv. Opt. Mat. *6*, 1701213.

20. Kempa, T., Farrer, R.A., Giersig, M., and Fourkas, J.T. (2006). Photochemical synthesis and multiphoton luminescence of monodisperse silver nanocrystals. Plasmonics *1*, 45–51.

21. Davies, R., Dinsdale, A., Gisby, J., Robinson, J., and Martin, A.M. (2002). MTDATA-thermodynamic and phase equilibrium software from the national physical laboratory. Calphad *26*, 229–271.

22. Fang, Z.Y., Zhen, Y.R., Neumann, O., Polman, A., de Abajo, F.J.G., Nordlander, P., and Halas, N.J. (2013). Evolution of light-induced vapor generation at a liquid-immersed metallic nanoparticle. Nano Lett. *13*, 1736–1742.

23. Lin, L.H., Peng, X.L., Mao, Z.M., Li, W., Yogeesh, M.N., Rajeeva, B.B., Perillo, E.P., Dunn, A.K., Akinwande, D., and Zheng, Y.B. (2016). Bubble-pen lithography. Nano Lett. *16*, 701–708.

24. Rajeeva, B.B., Lin, L.H., Perillo, E.P., Peng, X.L., Yu, W.W., Dunn, A.K., and Zheng, Y.B. (2017). High-resolution bubble printing of quantum dots. ACS Appl. Mater. Interfaces *9*, 16725–16733.

25. Rajeeva, B.B., Alabandi, M.A., Lin, L., Perillo, E.P., Dunn, A.K., and Zheng, Y. (2017). Patterning and fluorescence tuning of quantum dots with haptic-interfaced bubble printing. J. Mater. Chem. C *5*, 5693–5699.

26. Roy, B., Arya, M., Thomas, P., Jürgschat, J.K., Venkata Rao, K., Banerjee, A., Malla Reddy, C., and Roy, S. (2013). Self-assembly of mesoscopic materials to form controlled and continuous patterns by thermo-optically manipulated laser induced microbubbles. Langmuir *29*, 14733–14742.

27. Fujii, S., Fukano, R., Hayami, Y., Ozawa, H., Muneyuki, E., Kitamura, N., and Haga, M.-A. (2017). Simultaneous formation and spatial patterning of ZnO on ITO surfaces by local laser-induced generation of microbubbles in aqueous solutions of $[Zn(NH_3)_4]^{2+}$. ACS Appl. Mater. Interfaces *9*, 8413–8419.

28. Armon, N., Greenberg, E., Layani, M., Rosen, Y.S., Magdassi, S., and Shpaisman, H. (2017). Continuous nanoparticle assembly by a modulated photo-induced microbubble for fabrication of micrometric conductive patterns. ACS Appl. Mater. Interfaces *9*, 44214–44221.

29. Zhakeyev, A., Wang, P.F., Zhang, L., Shu, W.M., Wang, H.Z., and Xuan, J. (2017). Additive manufacturing: unlocking the evolution of energy materials. Adv. Sci. *4*, 1700187.

30. Thanh, N.T.K., Maclean, N., and Mahiddine, S. (2014). Mechanisms of nucleation and growth

of nanoparticles in solution. Chem. Rev. *114*, 7610–7630.

31. De Yoreo, J.J., and Vekilov, P.G. (2003). Principles of crystal nucleation and growth. Biomineralization *54*, 57–93.

32. Weiss, G.H., and Rubin, R.J. (1983). Random-walks—theory and selected applications. Adv. Chem. Phys. *52*, 363–505.

33. Zhao, C., Xie, Y., Mao, Z., Zhao, Y., Rufo, J., Yang, S., Guo, F., Mai, J.D., and Huang, T.J. (2014). Theory and experiment on particle trapping and manipulation via optothermally generated bubbles. Lab Chip *14*, 384–391.

34. Preuss, M., and Butt, H.J. (1999). Direct measurement of forces between particles and bubbles. Int. J. Miner. Process. *56*, 99–115.

35. Fielden, M.L., Hayes, R.A., and Ralston, J. (1996). Surface and capillary forces affecting air bubble-particle interactions in aqueous electrolyte. Langmuir *12*, 3721–3727.

36. Wang, L.H., and Harris, M.T. (2018). Stagnation point of surface flow during drop evaporation. Langmuir *34*, 5918–5925.

37. Xu, X.F., and Luo, J.B. (2007). Marangoni flow in an evaporating water droplet. Appl. Phys. Lett. *91*, https://doi.org/10.1063/1.2789402.

38. Shiba, F., and Okawa, Y. (2005). Relationship between supersaturation ratio and supply rate of solute in the growth process of monodisperse colloidal particles and application to AgHr systems. J. Phys. Chem. B *109*, 21664–21668.

39. Xiao, S., Hu, W., Luo, W., Wu, Y., Li, X., and Deng, H. (2006). Size effect on alloying ability and phase stability of immiscible bimetallic nanoparticles. Eur. Phys. J. B *54*, 479–484.

40. House, S.D.,, Bonifacio, C.S.,, Timoshenko, J.,, and Kunal, P. (2017). Computationally assisted STEM and EXAFS characterization of tunable Rh/Au and Rh/Ag bimetallic nanoparticle catalysts. Microsc. Microanal. *23* (S1), 2030–2031.

41. Chen, P.C., Liu, X.L., Hedrick, J.L., Xie, Z., Wang, S.Z., Lin, Q.Y., Hersam, M.C., Dravid, V.P., and Mirkin, C.A. (2016). Polyelemental nanoparticle libraries. Science *352*, 1565–1569.

42. Holewinski, A., Idrobo, J.C., and Linic, S. (2014). High-performance Ag-Co alloy catalysts for electrochemical oxygen reduction. Nat. Chem. *6*, 828–834.

43. Zugic, B., Wang, L.C., Heine, C., Zakharov, D.N., Lechner, B.A.J., Stach, E.A., Biener, J., Salmeron, M., Madix, R.J., and Friend, C.M. (2017). Dynamic restructuring drives catalytic activity on nanoporous gold-silver alloy catalysts. Nat. Mater. *16*, 558–564.

44. Li, H., Luo, L., Kunal, P., Bonifacio, C.S., Duan, Z.Y., Yang, J.C., Humphrey, S.M., Crooks, R.M., and Henkelman, G. (2018). Oxygen reduction reaction on classically immiscible bimetallics: a case study of RhAu. J. Phys. Chem. C *122*, 2712–2716.